

ENHANCEMENT OF CO(3–2)/CO(1–0) RATIOS AND STAR FORMATION EFFICIENCIES IN SUPERGIANT HII REGIONS

RIE E. MIURA^{1,2}, KOTARO KOHNO^{3,4}, TOMOKA TOSAKI⁵, DANIEL ESPADA^{1,6,9}, AKIHIKO HIROTA⁷, SHINYA KOMUGI¹, SACHIKO K. OKUMURA⁸, NARIO KUNO^{7,9}, KAZUYUKI MURAOKA¹⁰, SACHIKO ONODERA¹⁰, KOUICHIRO NAKANISHI^{1,6,9}, TSUYOSHI SAWADA^{1,6}, HIROYUKI KANEKO¹¹, TETSUHIRO MINAMIDANI⁷, KOSUKE FUJII^{1,2}, RYOHEI KAWABE^{1,6}

Draft version October 13, 2018

ABSTRACT

We present evidence that super giant HII regions (GHRs) and other disk regions of the nearby spiral galaxy, M33, occupy distinct locations in the correlation between molecular gas, Σ_{H_2} , and the star formation rate surface density, Σ_{SFR} . This result is based on wide field and high sensitivity CO(3–2) observations at 100 pc resolution. Star formation efficiencies (SFE), defined as $\Sigma_{\text{SFR}}/\Sigma_{\text{H}_2}$, in GHRs are found to be ~ 1 dex higher than in other disk regions. The CO(3–2)/CO(1–0) integrated intensity ratio, $R_{3-2/1-0}$, is also higher than the average over the disk. Such high SFE and $R_{3-2/1-0}$ can reach the values found in starburst galaxies, which suggests that GHRs may be the elements building up a larger scale starburst region. Three possible contributions to high SFEs in GHR are investigated: (1) the $I_{\text{CO}} - N(\text{H}_2)$ conversion factor, (2) the dense gas fraction traced by $R_{3-2/1-0}$, and (3) the initial mass function (IMF). We conclude that these starburst-like properties in GHRs can be interpreted by a combination of both a top-heavy IMF and a high dense gas fraction, but not by changes in the $I_{\text{CO}} - N(\text{H}_2)$ conversion factor.

Subject headings: galaxies: individual (M33) — ISM: clouds — (ISM:) HII regions — radio lines: ISM

1. INTRODUCTION

Large starburst systems are characterized by high star formation rates (SFR) (Kennicutt 1998). Recently, Daddi et al. (2010, hereafter D10) have suggested the existence of two different star formation (SF) regimes based on the so-called SF law (Schmidt 1959; Kennicutt 1989), the relation between the molecular gas (Σ_{H_2}) and SFR surface densities (Σ_{SFR}): *i*) a rapid mode of SF for starbursts, and *ii*) a long-lasting mode for disks. While the former mode is mostly found in active star forming galaxies, having about one dex higher SF efficiencies (SFE, defined as $\Sigma_{\text{SFR}}/\Sigma_{\text{H}_2}$), the latter is composed by relatively normal galaxies. It has been claimed that the difference

of these two regimes may be due to the different dense gas fractions, the effect of a top-heavy initial mass function (IMF) in starbursts (D10), or to the $I_{\text{CO}} - N(\text{H}_2)$ conversion factor (hereafter X_{CO} factor; e.g., Magdis et al. 2011).

Although not following a bimodal distribution, a large variation in SFE is known on resolved scales from hundreds of parsec to parsec scale in our Galaxy and other galaxies (e.g. Schruba et al. 2010; Onodera et al. 2010; Heiderman et al. 2010; Lada et al. 2012; Leroy et al. 2013; Lada et al. 2013). Leroy et al. (2013) suggested that the large scatter in SFE (0.3 dex) at kpc resolution in nearby galaxies. These can be attributed to different X_{CO} factors. These studies are still beyond the unit of SF, i.e., Giant Molecular Cloud (GMC), and their measurements average over kiloparsec scales including areas with very different physical conditions. At resolved GMC scales (several tens of parsec) the scatter on the SF law becomes even larger, which might be due to the spatial offsets between star forming regions and molecular clouds (Schruba et al. 2010; Onodera et al. 2010; Chen et al. 2010).

At even higher resolution such as molecular clump scale (parsec scale), the observed SFE for Galactic dense clumps exceeds the observed extragalactic predictions by factors of 17–50 (Heiderman et al. 2010). Such large variations in SFE can be attributed to the different volume density of individual clumps (Heiderman et al. 2010; Lada et al. 2012). However these Galactic studies corresponds to low mass star forming regions and do not elucidate the physical conditions of massive star forming regions, which is the main source in terms of energy output in starburst galaxies.

The main goal of this Paper is to investigate the underlying relation between molecular gas and SF at GMC scales, especially focusing on the massive SF. This allow

rie.miura@nao.ac.jp

¹ National Astronomical Observatory of Japan, 2-21-1 Osawa, Mitaka, Tokyo, 181-8588, Japan

² Department of Astronomy, The University of Tokyo, Hongo, Bunkyo-ku, Tokyo, 113-0033, Japan

³ Institute of Astronomy, School of Science, The University of Tokyo, Osawa, Mitaka, Tokyo 181-0015, Japan

⁴ Research Center for Early Universe, School of Science, The University of Tokyo, Hongo, Bunkyo, Tokyo, 113-0033, Japan

⁵ Joetsu University of Education, Yamayashiki-machi, Joetsu, Niigata, 943-8512, Japan

⁶ Joint ALMA Observatory, Alonso de Cordova 3107, Vitacura 763-0355, Santiago de Chile

⁷ Nobeyama Radio Observatory, Minamimaki, Minamisaku, Nagano, 384-1805, Japan

⁸ Department of Mathematical and Physical Sciences, Faculty of Science, Japan Womanfs University, Mejirodai 2-8-1, Bunkyo, Tokyo 112-8681, Japan

⁹ Department of Astronomical Science, The Graduate University for Advanced Studies (Sokendai), 2-21-1 Osawa, Mitaka, Tokyo 181-0015, Japan

¹⁰ Osaka Prefecture University, Gakuen 1-1, Sakai, Osaka 599-8531, Japan

¹¹ Department of Physics, Meisei University, Hino, Tokyo 191-8506, Japan

¹² Graduate School of Pure and Applied Sciences, Institute of Physics, University of Tsukuba, 1-1-1 Tennodai, Tsukuba, Ibaraki 305-8571, Japan

us to infer the properties of the building elements of starbursts. Super giant HII regions (GHRs), characterized by a $H\alpha$ luminosity of more than 10^{39} erg s $^{-1}$ and a size of more than 100 pc (Kennicutt et al. 1989), are arguably among the most important candidates to understand the SF process occurring at distant starburst systems because there is a close resemblance of properties between them. In fact, GHRs are often called “mini-starbursts” because they contain tens to hundreds of young clusters rich in O, B, Wolf-Rayet stars and are predicted to have quasi-instantaneous events of SF in a few Myr (e.g., Pellerin 2006). The majority of massive stars born in GHRs are expected to be formed inside 100 pc-scale giant molecular clouds (GMC; Mayya & Prabhu 1996).

Nearby extragalactic GHRs not only permit detailed studies of individual stars and their parent molecular gas but also of the SF law under these peculiar environmental conditions. M33 is the nearest spiral galaxy with the most luminous GHRs in the Local Group galaxies (LGGs), which makes it one of the best laboratories to study this problem. Its favourable inclination is also ideal to resolve the typical size of GMCs with less contamination of projected emission along the line of sight, unlike in our Galaxy. Another advantage over our Galaxy is that all GMCs are at the same distance.

We obtained wide field and high resolution single-dish mapping of the CO(3–2) emission toward M33 (Miura et al. 2012, hereafter Paper I), as part of the NRO MAGiC project (Tosaki et al. 2011; Komugi et al. 2011; Onodera et al. 2012). In Paper I, we identified 65 GMCs and classified them into four categories according to their spatial correlation with young (< 10–30 Myr-old) stellar groups (YSGs) and HII regions. This classification was interpreted as an evolutionary sequence of GMCs.

In this Paper we aim (1) to check whether the SF law holds around GHRs, (2) to compare the SF law with that in large scale starburst environments, and (3) to infer the origin of any peculiarity of the molecular gas properties and SF in GHRs. Note that although previous molecular SF law studies in M33 have been carried out using different CO transition lines at 80–200 pc resolution (e.g., Heyer et al. 2004; Onodera et al. 2010, 2012), a detailed SF law taking into account these peculiar regions has not been performed so far.

2. DATA

2.1. Molecular gas surface densities

We use ASTE 10-m CO(3–2) and NRO 45-m CO(1–0) data cubes. See Paper I for a description of the observations and data reduction. The observed regions are shown in Figure 1. However, note that in this Paper we have added CO(3–2) data for the northern inner kiloparsec region ($325'' \times 240''$; see Figure 1). The new observations were performed between November and December 2011, using the ASTE 10-m dish (Ezawa et al. 2004, 2008). The On-The-Fly mapping technique was employed to obtain the CO(3–2) data. The main beam efficiency is measured to be 0.5 ± 0.1 . The typical system temperatures in a single side band were 300 to 400 K. The spatial resolution of the final map is $25''$ (~ 100 pc) and the grid spacing $8''$. The data calibration and reduction were performed in a similar way to the previously obtained data for other fields of views (Paper I). Fur-

ther information on these new ASTE observations will be reported in detail in a forthcoming paper.

The rms per 2.5 km s $^{-1}$ velocity resolution (σ_{ch}) spans 16–32 mK, depending on the regions. The CO(3–2) and CO(1–0) integrated intensity maps are created over the same velocity range where emission was above $2\sigma_{\text{ch}}$. The rms of the integrated intensity maps (σ_{mom}) for each region is 0.16–0.88 K km s $^{-1}$ and 0.72–1.30 K km s $^{-1}$, for the CO(3–2) and CO(1–0) maps, respectively. Thus the sensitivity of CO(3–2) data is better by a factor of 1–5 (depending on the regions) than that of the CO(1–0) data.

2.2. Star Formation Rate

We use the same calibrated $H\alpha$ image and the *Spitzer* $24 \mu\text{m}$ data as in Paper I. In this Paper, we have applied a local background subtraction (e.g. Liu et al. 2011) for these data sets using the *HIIphot* package (Thilker et al. 2000). The extinction-corrected $H\alpha$ map was created using a linear combination of the two local background subtracted luminosities, and then the SFR per unit area was calculated using the equation (7) in Calzetti et al. (2007). The resultant SFR image at $5''.7$ resolution is shown in Figure 1. The resulting rms noise of the SFR maps is 6.5×10^{-5} $M_{\odot} \text{ yr}^{-1} \text{ kpc}^{-2}$, corresponding to an uncertainty of 4% on average. Finally the SFR image was convolved and regridded to a common angular resolution, $25''$, so that each data point corresponds to a resolution element when we do a pixel-to-pixel analysis of the SF law.

3. STAR FORMATION LAW IN GIANT HII REGIONS OF M33

First, we calculate the best linear fit in the form $\log \Sigma_{\text{SFR}} [M_{\odot} \text{ yr}^{-1} \text{ kpc}^{-2}] = \alpha \log I_{\text{CO}(3-2)} [\text{K km s}^{-1}] + \beta$ to all the data with $I_{\text{CO}(3-2)} > 2\sigma_{\text{mom}}$, and we obtain $\alpha = 1.04 \pm 0.14$ and $\beta = -2.21 \pm 0.03$. We use the ordinary least-squares (OLS) bisector fit following previous studies of the SF law (e.g., Bigiel et al. 2008) to be able to compare. The slope in the $\Sigma_{\text{SFR}}-I_{\text{CO}(3-2)}$ plot of M33 is close to unity as found in other studies (Iono et al. 2009; Wilson et al. 2012; Komugi et al. 2007). Our result confirms that the SF law with CO(3–2) is kept from GMC scales (100 pc) to large scales, over a variety of environments and physical conditions.

Next we investigate the SF law for regions close to GHRs. We present a $\Sigma_{\text{SFR}}-I_{\text{CO}(3-2)}$ plot in Figure 2. We compare regions with GHRs and without GHRs. We restrict to radii within 200 pc from the centre of the GHR to probe molecular gas potentially affected by the GHRs (Wilson et al. 1997). Our CO(3–2) observed regions include two of the most luminous GHRs in LGGs, NGC 595 and NGC 604. The bisector fit for regions close to GHRs is $\alpha = 1.11 \pm 0.21$ and $\beta = -1.28 \pm 0.09$ and for the non-GHRs $\alpha = 1.23 \pm 0.12$ and $\beta = -2.33 \pm 0.03$. While the slopes are comparable within the uncertainties, we find that there is a remarkable offset in the intercept of ~ 1 dex.

Because this is a pixel-to-pixel plot with ~ 100 pc scale, this offset might be caused by the drift of young clusters from their parent GMCs as suggested by Schrubba et al. (2010) and Onodera et al. (2010). In order to check if this possibility contributes to the difference in SFR be-

tween GHR and non-GHR points, we plot in Figure 3 the SFR and CO luminosities averaged over each GMC from our CO(3–2) GMC catalog (Paper I; Miura et al. in preparation). Note that most of the young star forming regions associated with each GMC are still within the GMC boundary (Paper I). The star symbols are the data points for GHRs, while the other filled circles represent each of the four evolutionary stages of GMCs in M33: Type A GMCs show no sign of massive SF, Type B are associated only with relatively small HII regions, Type C with both HII regions and relatively young (< 10 Myr) YSGs, and Type D with both HII regions and relatively old (> 10 Myr old) YSGs (Paper I).

We find a large scatter in the fit for the M33 GMCs. Although the SF law is maintained on GMC scales, part of the scatter may arise from differences in the evolutionary stages of the GMCs. The data points for Type A and B are located preferentially below the fit, while those for Type C and Type D, distribute around the fitted line. The data points for NGC 604 and NGC 595 are still 1dex higher than the ones for non-GHRs, even in the SF law for individual GMCs. This suggests that high SFEs are not caused by an offset between the molecular gas and the SF regions.

We note that GMC-27 also seems to have a relevant offset with respect to the fit. GMC-27 is located at the vicinity of the GHR NGC 604, but it was distinguishable from the nearby GMC associated with NGC 604 by a large velocity difference of 20 km s^{-1} (Miura et al. 2010). It is necessary to avoid the possible contamination in the star formation tracers ($\text{H}\alpha$ emission and $24 \mu\text{m}$) along the line of sight, but it is not possible due to lack of velocity information. Thus the relatively high SFR at GMC-27 is likely an overestimation due to contamination by the neighbouring GHR.

4. COMPARISON WITH OTHER GALAXIES

A bimodal behavior of rapid vs slow SF modes was found in external galaxies (D10; Komugi et al. 2005): *normal* star forming galaxy such as spiral and BzK galaxies (Daddi et al. 2004), and starburst galaxies such as luminous infrared and submillimeter galaxies, respectively. In this section, we compare the SF law for the GHRs in M33 with that in the external galaxies.

Figure 4 shows the SF law plot of M33 together with data of other nearby and distant galaxies in D10. The molecular gas density for M33 was derived using the following equation: $\Sigma_{\text{H}_2} [M_{\odot} \text{ pc}^{-2}] = 4.81 I_{\text{CO}(3-2)} X_{\text{CO}} (R_{3-2/1-0})^{-1}$, where we assume that the X_{CO} factor in M33 is the Galactic value, $X_{\text{CO,Gal}} = (3 \pm 1) \times 10^{20} \text{ cm}^{-2} (\text{K km s}^{-1})^{-1}$ (Strong et al. 1988), and a fixed conversion factor from $I_{\text{CO}(3-2)}$ to $I_{\text{CO}(1-0)}$, $R_{3-2/1-0} = 0.4$, corresponding to the average line ratio over the M33 GMCs (Paper I). We account for Helium (a factor of ~ 1.36) but not for the inclination of the galaxy.

We plot data for the GHR and non-GHR domains separately: data points for GHRs are shown as red filled stars, while for non-GHR as blue contours. The solid line corresponds to the fit to normal galaxies (slope of 1.42) and the dashed line is the same relation offset by 0.9 dex to fit starburst galaxies. These represent the “sequence of disks” and “sequence of starbursts”, respectively. The

method to estimate Σ_{H_2} is different in the definitions among the different galaxy samples, but are not large enough to explain the offset of 0.9 dex between the two sequences (D10).

We find that the majority of data points in M33 are aligned along the sequence of disks, but the SFRs in GHRs are much higher and reach the sequence of starbursts. For reference, we also plot other bright HII regions in M33: NGC 592, NGC 588 and IC131. Their SFR is measured as in § 2.2, but we calculate an upper limit of Σ_{H_2} from the CO(1–0) observations in Rosolowsky et al. (2007) because these are outside of our CO(3–2) mapping area. These upper limits also lie along the starburst sequence.

In summary, the SFEs in GHRs are ~ 1 dex higher than that in *normal* disk regions. Wilson & Matthews (1995) previously reported that NGC 604 and NGC 595 had a factor of 3 higher SFE than the average over the disk. The differences between our result and them might come from the different definition and method to calculate stellar masses and SFEs. Their definition of SFE is given as mass of optically visible stars formed per GMC mass, while ours include the contribution from embedded stars, derived from a combination of the $\text{H}\alpha$ and $24 \mu\text{m}$ data. Also, we employ pixel-to-pixel analysis, which focus on the molecular gas at the very vicinity of the star forming region.

5. PROPERTIES OF GIANT MOLECULAR CLOUDS AROUND GIANT HII REGIONS

The offset between the two sequences has been argued to be related to a different physical origin due to (1) a different X_{CO} factor, (2) the fraction of dense molecular gas, or (3) the effect of a top-heavy IMF in starbursts (§ 1). In the following subsections, we confront the peculiarity of high SFE in GHRs against the three different explanations above.

5.1. Is There any Difference in the X_{CO} Factor?

A general method to derive the X_{CO} factor is to compare the virial masses (M_{vir}) and the CO(1–0) luminosity of a cloud. In order to examine the relation between M_{vir} and CO(1–0) luminosities in M33, we use the GMC catalog in Rosolowsky et al. (2007) because their data has a resolution high enough to resolve the typical size of a GMC (~ 50 pc). As in their catalog, we calculated the M_{vir} using the equation in Wilson & Scoville (1990). The GMC sizes were derived using $D_{\text{pc}} = \sqrt{A_{\text{maj}} \times A_{\text{min}}}$, where A_{maj} and A_{min} are the major and minor axes. D_{pc} spans from 50 pc to 160 pc.

A plot of the M_{vir} as a function of the molecular mass (M_{mol}) is shown in Figure 5, which is useful to derive the X_{CO} factor. Here we use the M_{mol} from Rosolowsky et al. (2007), but using $X_{\text{CO,Gal}}$. Star symbols in Figure 5 represent data for GHRs, NGC 595 and NGC 604. The best fit to all data is $M_{\text{vir}} = (1.03 \pm 0.08) M_{\text{mol}}$ if we take absolute errors into account. The X_{CO} factor for each cloud in M33 is expressed as $X_{\text{CO}} = X_{\text{CO,Gal}} \frac{M_{\text{vir}}}{M_{\text{mol}}}$ (Wilson 1995). Thus the fit suggests that the X_{CO} factor of $(3.1 \pm 0.2) \times 10^{20} \text{ cm}^{-2} (\text{K km s}^{-1})^{-1}$ is likely the best value to estimate the M_{mol} assuming that the virial equilibrium holds.

If we interpret that the difference values between

GMCs associated with the GHRs and ones with non-GHRs, the X_{CO} factor is slightly lower in these GHRs than other fields: their virial parameter is $M_{\text{vir}}/M_{\text{mol}} \sim 0.55 \pm 0.20$, which corresponds to a X_{CO} factor of $(1.5 \pm 0.2) \times 10^{20} \text{ cm}^{-2} (\text{K km s}^{-1})^{-1}$. When this X_{CO} factor is applied, the calculated molecular mass for the GHRs decreases compared to the obtained value with the $X_{\text{CO,Gal}}$ factor, and thus this results in an even higher SFE. Another interpretation is that SF clouds are more gravitationally bound than as data points for GHRs are below the virial equilibrium line. At any cases, the X_{CO} factor does not explain why the SFEs in GHRs are high.

5.2. Is SFE Higher in Dense Gas?

The $R_{3-2/1-0}$ provides a rough estimation of the gas density (n_{H_2}) and kinetic temperature (T_{kin}) (e.g., Minamidani et al. 2008). Figure 6 shows the plot of the $R_{3-2/1-0}$ versus SFE derived from CO(3–2) and CO(1–0) (hereafter $\text{SFE}_{\text{H}_2(\text{CO } J=3-2)}$ and $\text{SFE}_{\text{H}_2(\text{CO } J=1-0)}$). The CO(1–0) molecular gas surface densities are calculated using $\Sigma_{\text{H}_2} = 4.81 I_{\text{CO}(1-0)} X_{\text{CO,Gal}}$.

In the $\text{SFE}_{\text{H}_2(\text{CO } J=3-2)} - R_{3-2/1-0}$ plot, we find that the non-GHRs data points show a nearly flat distribution, which is consistent with other studies (Warren et al. 2010). On the contrary, a positive correlation is apparent in the $\text{SFE}_{\text{H}_2(\text{CO } J=1-0)} - R_{3-2/1-0}$ plot. This trend is similar to that in the inner kiloparsec of M83, known to host a starburst nucleus (Muraoka et al. 2007). When taking it into account that $R_{3-2/1-0}$ can be a diagnostic of dense gas fraction at GMC scale (Minamidani et al. 2008), these plots suggest that the SFE of the dense molecular gas is independent of the dense gas fraction, while the SFE of the more diffuse molecular gas is enhanced in dense gas regions.

In both plots the SFE and $R_{3-2/1-0}$ of GHRs are higher than in non-GHRs. Their $R_{3-2/1-0} \sim 1$ suggests that these GMCs are dense and warm. We calculate how different the physical properties between GHRs and non-GHRs are according to the large velocity gradient (LVG) approximation, by using the $^{12}\text{CO}(1-0)/^{13}\text{CO}(1-0)$ ($R_{13/12(J=1-0)}$), $^{12}\text{CO}(2-1)/^{13}\text{CO}(2-1)$ ($R_{13/12(J=2-1)}$) and $^{12}\text{CO}(3-2)/^{12}\text{CO}(2-1)$ ratios ($R_{3-2/2-1}$) of seven GMCs in Wilson et al. (1997). This follows the same prescription as in Minamidani et al. (2008), which was used for the LMC where the metallicity is similar to that of M33. Wilson et al. (1997)’s observations have a similar beam size except $^{13}\text{CO}(1-0)$ observations ($55''$), and thus their $R_{13/12(J=1-0)}$ is calculated with the resolution of $^{13}\text{CO}(1-0)$ data. All seven GMCs are covered by our CO(3–2) observations and named in Paper I as GMC-1, 5, 15, 17, 18, 27, and 72. Note that their alternative names in Wilson et al. (1997) are NGC604-2, MC1, MC32, MC19, MC13, NGC604-4 and MC20, respectively.

The $R_{3-2/1-0}$ of the corresponding position for the seven GMCs are measured from the CO(3–2) and CO(1–0) maps of the individual GMC in Paper I. In Figure 7 we present the LVG analysis from the four line ratios $R_{3-2/1-0}$ (black solid line), $R_{13/12(J=1-0)}$ (gray dotted-dashed line), $R_{13/12(J=2-1)}$ (green dotted line) and $R_{3-2/2-1}$ (blue dashed line). Since the lines for $R_{3-2/1-0}$ and $R_{3-2/2-1}$ ratios well overlapped on the

LVG plane, in general our $R_{3-2/1-0}$ measurements are consistent with $R_{3-2/2-1}$ in Wilson et al. (1997). However, we cannot obtain solutions for GMC-17 and GMC-1 (NGC 604) with these four line ratios (even with the data of Wilson et al. 1997). Because the $R_{13/12(J=1-0)}$ ratio traces the properties of a larger portion of the molecular cloud, this cause large uncertainty due to averaging and we preferred to use $R_{13/12(J=2-1)}$ in the analysis rather than $R_{13/12(J=1-0)}$. If we exclude the $R_{13/12(J=1-0)}$ ratios in GMC-17 and GMC-1 we obtain $n_{\text{H}_2} \sim (1-2) \times 10^3 \text{ cm}^{-3}$ and $T_{\text{kin}} = 10-20 \text{ K}$ for non-GHRs (5, 15, 17, 18, 27, and 28), while $n_{\text{H}_2} > 2 \times 10^4 \text{ cm}^{-3}$ and $T_{\text{kin}} > 100 \text{ K}$ for GHR (GMC-1).

In summary, the GMCs in GHRs are about 10–20 times denser and warmer than the ones in non-GHRs. Since free-fall time is inversely proportional to the density square root, the dense molecular gas would tend to collapse to form stars rapidly, which would result in a higher SFE : $\text{SFE} \propto \text{SFR}/(M_{\text{gas}}/\tau_{\text{ff}})$ (Krumholz et al. 2012). For densities three times larger, the SFE would increase by a factor of 3–4. Therefore the high SFE in GHRs can be partly due to a larger local dense gas fraction.

5.3. Top-heavy IMF in GHRs

The IMFs in NGC 604 and NGC 595 are previously found to be flatter ($\alpha = 1.88$ and 1.92 ¹³; Drissen et al. 1993) than the Salpeter IMF ($\alpha = 2.35$), similar to those observed in starburst galaxies (e.g., Rieke et al. 1980). We estimated the SFR with different IMFs for the GHRs and the disk, using the stellar population models of Starburst99¹⁴ (Leitherer et al. 1999). For non-GHRs we have used the Starburst99 default parameters of a constant SF model, which consists of a Salpeter IMF with mass limits of 0.1–100 M_{\odot} , solar metallicity $Z_{\odot} = 0.02$ and a 100 Myr duration model of constant SF. For GHRs we adopted the same parameters except for the IMF. The conversion from the (extinction-free) $\text{H}\alpha$ luminosity, $L(\text{H}\alpha)$ [ergs s⁻¹], to SFR [$M_{\odot} \text{ yr}^{-1}$], with a Salpeter IMF is $\text{SFR} = 6.31 \times 10^{-42} L(\text{H}\alpha)$ in case of IMF of 1.88, and $\text{SFR} = 1.76 \times 10^{-42} L(\text{H}\alpha)$, and in case of IMF of 1.92, $\text{SFR} = 1.91 \times 10^{-42} L(\text{H}\alpha)$. The SFRs derived with a flatter IMF are a factor of 3–4 smaller than those with a Salpeter IMF. This result does not considerably change even if we use the starburst model in the Starburst99 instead of constant SF model. Therefore, a flatter IMF in GHRs may contribute to the SFE’s 1 dex offset.

6. IMPLICATIONS

The two different regimes on the SF law plot of GHRs and non-GHRs may arise from the contribution of a different fraction of dense molecular gas and a top-heavy IMF, but not from a different X_{CO} factor. In this section, we provide a scenario in which the combination of these two factors may explain the high SFE and $R_{3-2/1-0}$ found in GHRs.

A top-heavy IMF is characterized by an overabundance of massive stars. Once massive stars are born in a cluster, they produce intense ionization photons and stellar

¹³ The IMF is expressed as $dN \propto m^{-\alpha} dm$, where dN is the number of stars with masses in a range of m to $m + dm$.

¹⁴ See <http://www.stsci.edu/science/starburst99>

winds, and then finally become supernovae. These radiative and mechanical energetic input can destroy the structure of the parental molecular clouds, which may suppress subsequent SF (negative feedback). Contrary to this, the shock front emerges and compresses the surrounding gas into a very dense layer where second SF is triggered (positive feedback). SF regions where positive feedback overcome the negative one has been witnessed in M33 as well as in our Galaxy (e.g., Beuther et al. 2012). In the two GHRs, NGC 604 and NGC 595, dense molecular gas was detected at the periphery of the HII regions where massive stars are born but molecular gas in its center is scarce (e.g., Tosaki et al. 2007; Miura et al. 2010; Relaño & Kennicutt 2009).

According to Hosokawa & Inutsuka (2006), the gas swept up to the layer around an expanding HII region (M_{sh}) is proportional to the ionizing photon rate (Q^*) when a constant initial ambient gas density is assumed. We calculated the Q^* for the 18 M33 YSGs, whose ages are estimated to be less than 10 Myr by counting the amount of O stars from our YSG catalog (Paper I), and assuming a standard value of Q^* for each stellar type (Martins et al. 2005). The calculated Q^* per YSG spans $(1-39) \times 10^{50}$ photons s^{-1} , and among which those in the two GHRs are at least 2–30 times larger than in other HII regions. In derivation of the M_{sh} from the Q^* , the scaling relations introduced in equations (39)–(41) of Hosokawa & Inutsuka (2006) is used and a classical HII region created by a single star with a mass of $100 M_{\odot}$ is adopted as a standard model (Hosokawa & Inutsuka 2006). In the uniform ambient density of 10^3 cm^{-3} , the molecular gas of $(3-18) \times 10^5 M_{\odot}$ can be accumulated in the shell within 3–4 Myr in the two GHRs. This is 2–30 times larger in the GHRs than in other HII regions.

This estimation is for the case of star formation under a uniform ambient density. The estimated M_{sh} depends in practice on physical conditions such as the ambient (pre-existing) density structure, stellar types and distribution (Hosokawa & Inutsuka 2006). For instance, the GHRs are characterized by complex distributions such as filaments, shells and bubbles (“champagne flow”; Tenorio-Tagle et al. 2006). In these cases, the ionization front rapidly erodes the parental cloud and only a part of the mass is swept-up and remains within the shell, which might result in smaller M_{sh} (Hosokawa & Inutsuka 2005). Although the use of refined numerical simulations is needed, this suggests that a larger amount of molecular clouds is accumulated in GHRs than in normal HII regions, which shields the FUV radiation field. In this way the subsequent SF occurs efficiently in a short time scale and would result in such high SFE in GHRs.

Although we have focused only on feedback via the expanding HII region, we note that the material for new stars can survive and the gas densities become larger even if the stellar feedback via supernova explosion is considered. For example, 30 Doradus is the brightest GHR in LGGs and many SNe reside. On the other hand, no candidates of SN remnant has been found at the vicinity of the central clusters of NGC 604 (Ghavamian et al. 2005). The 30 Doradus nebula is associated with CO molecular clouds with a total mass of $\sim 4 \times 10^5 M_{\odot}$ at the ridge of the central cluster (Johansson et al. 1998), in which the fragmentation has occurred to form dense

clumps and consequently new stars (Indebetouw et al. 2013). These molecular clouds have survived against the strong radiation from the central cluster and might be compressed by the pressure of the warm HII gas or the hot gas generated by shock heating from stellar winds and SNe (Pellegrini et al. 2011; Lopez et al. 2011). The swept-up molecular clouds could survive possibly because each fragment contracts to a dense clump, the column density increases and molecules will be protected against strong radiation (Hosokawa & Inutsuka 2007).

7. SUMMARY

In this Paper, we have studied the SF law and SFEs in the GHRs and other disk regions of M33, based on wide field and high sensitivity CO(3 – 2) and CO(1 – 0) observations at 100 pc resolution. We have examined three possibilities to contribute to the high SFEs in GHRs, such as X_{CO} factor, IMF and dense molecular gas fraction. Our results are the following:

1. We found high SFEs and $R_{3-2/1-0}$ in the molecular clouds around GHRs. SFEs differs about one dex from that of other disk regions in M33. Such high SFEs in GHRs is comparable to that in more distant starburst systems.
2. We examined a possible variation of the X_{CO} factor between the GHRs and other disk regions to explain that the X_{CO} factor does not contribute to the high SFE in M33 GHRs. We used the relation between virial masses and molecular masses and found that the estimated X_{CO} factor of GHRs are lower than that of other regions by a factor of 2.
3. The correlations between $R_{3-2/1-0}$ and SFE show a clear positive correlation. This suggests that the dense gas fraction traced by $R_{3-2/1-0}$ is correlated to SFE. To quantify this, we also conducted the LVG analysis for seven M33 GMCs including a GMC associated with GHR and showed that the densities in GHRs are a factor of 3–4 larger than the other GMCs associated with normal HII regions. This suggests that the variation in dense gas fraction can partially explain the high SFE in GHRs.
4. The SFR is calculated by adopting a top-heavy IMF in GHRs while a Salpeter IMF in other regions, using the Starburst99 program, which resulted in a difference of a factor of 3–4. This suggests that a flatter IMF in GHR than in other regions partially contributes to the SFE’s 1 dex offset.
5. We conclude that the high SFE at the GHRs can be interpreted by a combination of a different IMF and a larger fraction of dense molecular gas, but not due to a different X_{CO} conversion factor.
6. We suggest a scenario that the parental molecular gas would tend to get denser in the accumulated gas around the first generation stars, while to be rapidly consumed by SF, eroded and dissipated due to more massive stars in GHRs. This results in high

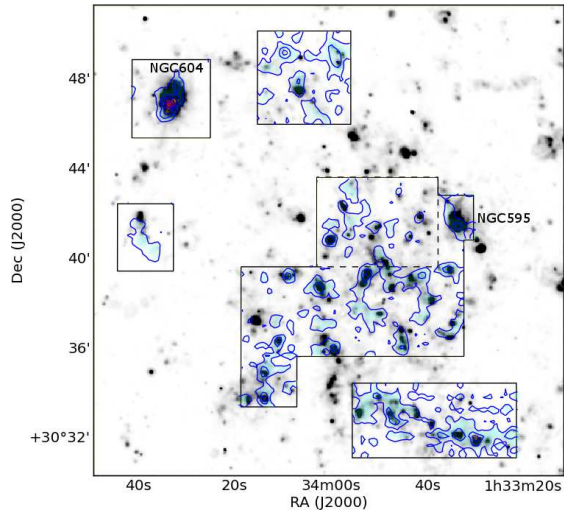


FIG. 1.— The CO(3–2) integrated intensity map of M33 (filled contour), overlaid on the grey scale SFR image. Contour levels are 1, 3, 5, 7, and 9 K km s^{-1} . The black boxes represent the observed regions in CO(3–2) emission presented in Paper I. The dashed box is the newly observed region.

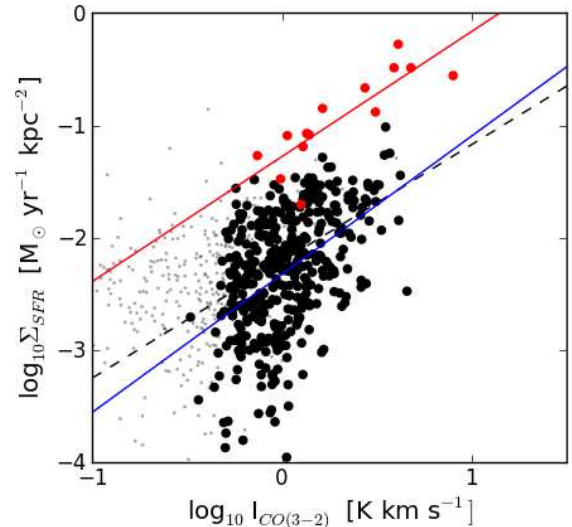


FIG. 2.— Comparison between the CO(3–2) intensities and SFR surface densities for the GHRs (red) and for the non-GHR (black), in a logarithmic scale. Data points where the intensity is lower than 2σ are shown in gray. The OLS fits to the data ($> 2\sigma$) for all regions, GHRs and non-GHRs are shown as a dashed line, red, and blue solid lines, respectively.

SFE and densities. We also suggest that this scenario localized around GHRs can be applied to the distant starburst systems where lack of resolution prevent us from resolving the building elements of the starburst.

We gratefully acknowledge the contributions of the ASTE staff to the development and operation of the telescope. The ASTE project is driven by NRO, a branch of NAOJ, in collaboration with University of Chile, and Japanese institutes including University of Tokyo, Nagoya University, Osaka Prefecture University, Ibaraki University, Hokkaido University and Joetsu University of Education.

REFERENCES

- Bertoldi, F. 1989, *ApJ*, 346, 735
 Beuther, H., Tackenberg, J., Linz, H., et al. 2012, *A&A*, 538, A11
 Bigiel, F., Leroy, A., Walter, F., et al. 2008, *AJ*, 136, 2846
 Calzetti, D., Kennicutt, R. C., Engelbracht, C. W., et al. 2007, *ApJ*, 666, 870
 Chen, C.-H. R., Indebetouw, R., Chu, Y.-H., et al. 2010, *ApJ*, 721, 1206
 Daddi, E., Cimatti, A., Renzini, A., et al. 2004, *ApJ*, 617, 746
 Daddi, E., Elbaz, D., Walter, F., et al. 2010, *ApJ*, 714, L118
 Drissen, L., Moffat, A. F. J., & Shara, M. M. 1993, *AJ*, 105, 1400
 Ezawa, H., Kawabe, R., Kohno, K., & Yamamoto, S. 2004, in *Society of Photo-Optical Instrumentation Engineers (SPIE) Conference Series*, Vol. 5489, Society of Photo-Optical Instrumentation Engineers (SPIE) Conference Series, ed. J. M. Oschmann Jr., 763–772
 Ezawa, H., Kohno, K., Kawabe, R., et al. 2008, in *Society of Photo-Optical Instrumentation Engineers (SPIE) Conference Series*, Vol. 7012, Society of Photo-Optical Instrumentation Engineers (SPIE) Conference Series
 Ghavamian, P., Blair, W. P., Long, K. S., et al. 2005, *AJ*, 130, 539
 Heiderman, A., Evans, II, N. J., Allen, L. E., Huard, T., & Heyer, M. 2010, *ApJ*, 723, 1019
 Heyer, M. H., Corbelli, E., Schneider, S. E., & Young, J. S. 2004, *ApJ*, 602, 723
 Hosokawa, T., & Inutsuka, S.-i. 2005, *ApJ*, 623, 917
 —. 2006, *ApJ*, 646, 240
 —. 2007, *ApJ*, 664, 363
 Indebetouw, R., Brogan, C., Chen, C.-H. R., et al. 2013, *ApJ*, 774, 73
 Iono, D., Wilson, C. D., Yun, M. S., et al. 2009, *ApJ*, 695, 1537
 Johansson, L. E. B., Greve, A., Booth, R. S., et al. 1998, *A&A*, 331, 857
 Kennicutt, Jr., R. C. 1989, *ApJ*, 344, 685
 —. 1998, *ApJ*, 498, 541
 Kennicutt, Jr., R. C., Edgar, B. K., & Hodge, P. W. 1989, *ApJ*, 337, 761
 Komugi, S., Kohno, K., Tosaki, T., et al. 2007, *PASJ*, 59, 55
 Komugi, S., Sofue, Y., Nakanishi, H., Onodera, S., & Egusa, F. 2005, *PASJ*, 57, 733
 Komugi, S., Tosaki, T., Kohno, K., et al. 2011, *PASJ*, 63, 1139
 Krumholz, M. R., Dekel, A., & McKee, C. F. 2012, *ApJ*, 745, 69
 Lada, C. J., Forbrich, J., Lombardi, M., & Alves, J. F. 2012, *ApJ*, 745, 190
 Lada, C. J., Lombardi, M., Roman-Zuniga, C., Forbrich, J., & Alves, J. F. 2013, *ApJ*, 778, 133
 Leitherer, C., Schaerer, D., Goldader, J. D., et al. 1999, *ApJS*, 123, 3
 Leroy, A. K., Walter, F., Sandstrom, K., et al. 2013, *AJ*, 146, 19
 Liu, G., Koda, J., Calzetti, D., Fukuhara, M., & Momose, R. 2011, *ApJ*, 735, 63
 Lopez, L. A., Krumholz, M. R., Bolatto, A. D., Prochaska, J. X., & Ramirez-Ruiz, E. 2011, *ApJ*, 731, 91
 Magdis, G. E., Daddi, E., Elbaz, D., et al. 2011, *ApJ*, 740, L15
 Martins, F., Schaerer, D., & Hillier, D. J. 2005, *A&A*, 436, 1049
 Mayya, Y. D., & Prabhu, T. P. 1996, *AJ*, 111, 1252
 Minamidani, T., Mizuno, N., Mizuno, Y., et al. 2008, *ApJS*, 175, 485
 Miura, R., Okumura, S. K., Tosaki, T., et al. 2010, *ApJ*, 724, 1120

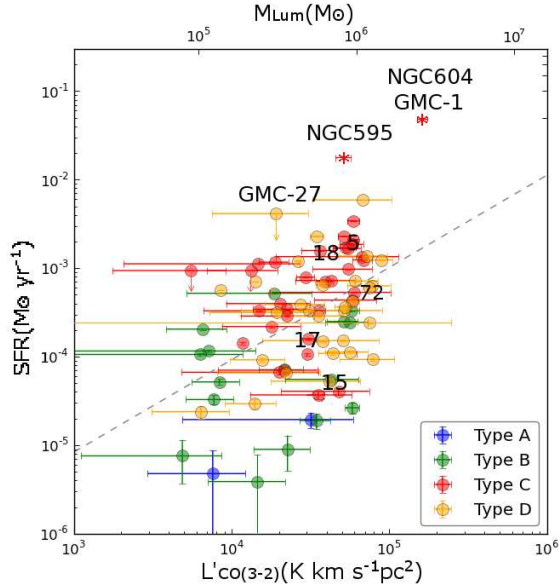


FIG. 3.— Comparison between the CO(3–2) luminosities and SFR surface densities for the two GMCs associated with GHRs, NGC 604 and NGC 595, as well as M33 GMCs in the four different evolutionary stages from Paper I are indicated in color code. The dashed line represents the best fit to all these data points. The GMCs used in the LVG-analysis in Figure 7 are labeled: GMC-1 (associated with the GHR NGC 604), GMC-5, 15, 17, 18, 27 and 72.

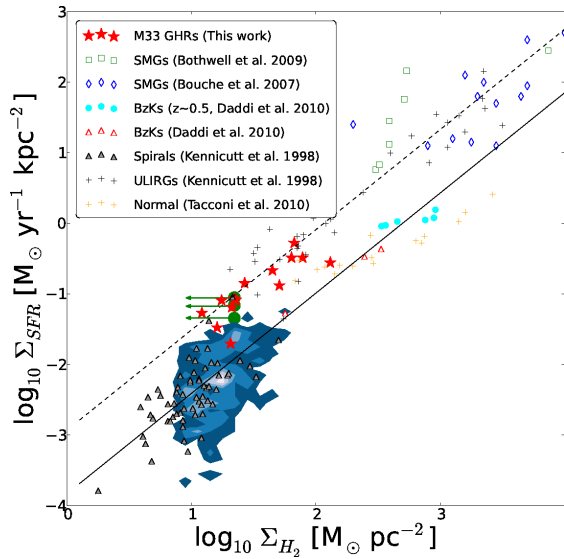


FIG. 4.— The SFR vs molecular gas surface densities for GHRs (red filled stars, NGC604 and NGC595) and for non-GHRs (blue filled contour) in M33, compared with that of other galaxies from Daddi et al. (2010, and references therein). Contour levels are 1, 3, 5, 7, and 9 independent data points, per 0.05 dex cell. Green circles represent other GHRs in M33, with the molecular gas mass estimated from the CO(1–0) data (Rosolowsky et al. 2007).

Miura, R. E., Kohno, K., Tosaki, T., et al. 2012, ApJ, 761, 37
 Muraoka, K., Kohno, K., Tosaki, T., et al. 2007, PASJ, 59, 43
 Onodera, S., Kuno, N., Tosaki, T., et al. 2010, ApJ, 722, L127
 —, 2012, PASJ, 64, 133
 Pellegrini, E. W., Baldwin, J. A., & Ferland, G. J. 2011, ApJ, 738, 34
 Pellerin, A. 2006, AJ, 131, 849
 Relaño, M., & Kennicutt, Jr., R. C. 2009, ApJ, 699, 1125

Rieke, G. H., Lebofsky, M. J., Thompson, R. I., Low, F. J., & Tokunaga, A. T. 1980, ApJ, 238, 24

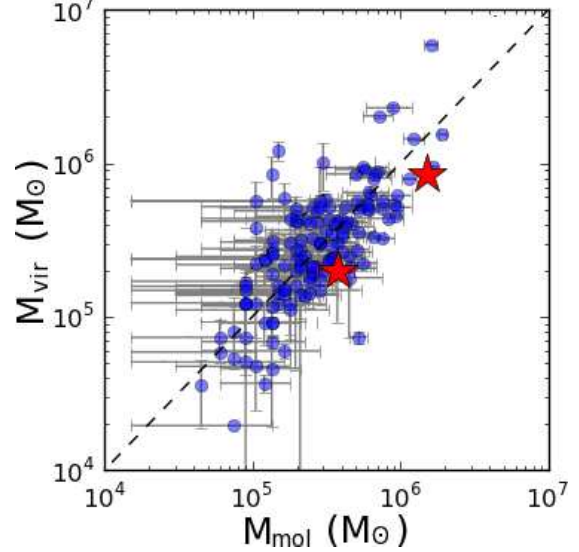


FIG. 5.— Plot of the virial mass of the M33 GMCs as a function of the molecular mass. These are based on the CO(1–0) GMC catalog with a resolution of ~ 50 pc (Rosolowsky et al. 2007). Star symbols represent GHRs. The dashed line indicates the case where the virial equilibrium holds.

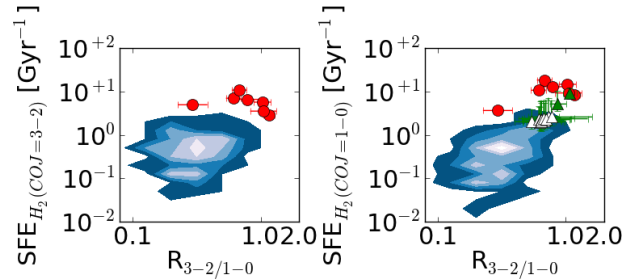


FIG. 6.— Plot of the $R_{3-2/1-0}$ versus $SFE_{H_2(CO J=3-2)}$ (left) and $SFE_{H_2(CO J=1-0)}$ (right). Data for GHRs are shown as red points, while that for non-GHRs as blue contours. Contour levels are 1, 3, 5, 7 and 9 independent data points per 0.05 dex cell. Data points where error are better than 40% are shown. The data points in several annuli of M83 are shown as green filled (unfilled) triangles, representing the center (disk)(Muraoka et al. 2007).

Rosolowsky, E., Keto, E., Matsushita, S., & Willner, S. P. 2007, ApJ, 661, 830
 Sandford, II, M. T., Whitaker, R. W., & Klein, R. I. 1982, ApJ, 260, 183
 Schmidt, M. 1959, ApJ, 129, 243
 Schrubba, A., Leroy, A. K., Walter, F., Sandstrom, K., & Rosolowsky, E. 2010, ApJ, 722, 1699
 Strong, A. W., Bloemen, J. B. G. M., Dame, T. M., et al. 1988, A&A, 207, 1
 Tenorio-Tagle, G., Muñoz-Tuñón, C., Pérez, E., Silich, S., & Telles, E. 2006, ApJ, 643, 186
 Thilker, D. A., Braun, R., & Waltherbos, R. A. M. 2000, AJ, 120, 3070
 Tosaki, T., Miura, R., Sawada, T., et al. 2007, ApJ, 664, L27
 Tosaki, T., Kuno, N., Onodera, S., et al. 2011, PASJ, 63, 1171
 Warren, B. E., Wilson, C. D., Israel, F. P., et al. 2010, ApJ, 714, 571
 Wilson, C. D. 1995, ApJ, 448, L97
 Wilson, C. D., & Matthews, B. C. 1995, ApJ, 455, 125
 Wilson, C. D., & Scoville, N. 1990, ApJ, 363, 435
 Wilson, C. D., Walker, C. E., & Thornley, M. D. 1997, ApJ, 483, 210
 Wilson, C. D., Warren, B. E., Israel, F. P., et al. 2012, MNRAS, 424, 3050

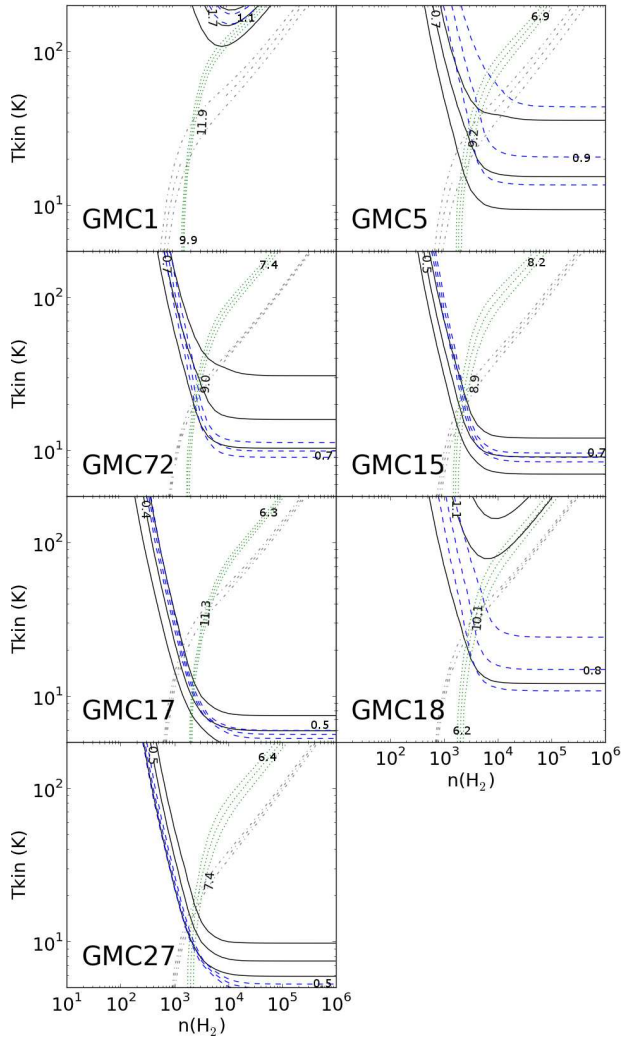


FIG. 7.— Kinetic temperature (T_{kin}) vs molecular hydrogen density ($n(\text{H}_2)$) plots for seven GMCs, using the LVG approximation. Gray dotted-dashed, green dotted, blue dashed and black solid lines indicate indicate $R_{13/12}(J=1-0)$, $R_{13/12}(J=2-1)$, $R_{3-2/2-1}$ and $R_{3-2/1-0}$ ratios, respectively. The values of each ratio are labeled in their corresponding lines. The three lines for each ratio indicate the line ratio with the intensity calibration errors ($\pm 1\sigma$). Acceptable values for T_{kin} and $n(\text{H}_2)$ are the region in which these four lines overlap within the intensity calibration errors.